Acta Crystallographica Section D
Biological Crystallography
ISSN 0907-4449

Structure of the *Methanothermobacter thermautotrophicus* exosome RNase PH ring

C. Leong Ng,*‡ David G. Waterman,§ Alfred A. Antson and Miguel Ortiz-Lombardía*¶

York Structural Biology Laboratory, Chemistry Department, University of York, York YO10 5YW, England

‡ Current address: Structural Studies Division, MRC Laboratory of Molecular Biology, Hills Road, Cambridge CB2 0QH, England.
§ Current address: Macromolecular Crystallography, Diamond Light Source Ltd, Harwell Science and Innovation Campus, Didcot, Oxfordshire OX11 0DE, England.
¶ Current address: Architecture et Fonction des Macromolécules Biologiques UMR6098, CNRS, Universités d'Aix-Marseille I & II, Case 932, 163 Avenue de Luminy, 13288 Marseille CEDEX 9, France.

Correspondence e-mail: clng@mrc-lmb.cam.ac.uk, miguel@afmb.univ-mrs.fr

Received 9 December 2009
Accepted 23 January 2010

PDB Reference: exosome RNase PH ring, 2wnr.

The core of the exosome, a versatile multisubunit RNA-processing enzyme found in archaea and eukaryotes, includes a ring of six RNase PH subunits. This basic architecture is homologous to those of the bacterial and archaeal RNase PHs and the bacterial polynucleotide phosphorylase (PNPase). While all six RNase PH monomers are catalytically active in the homohexameric RNase PH, only half of them are functional in the bacterial PNPase and in the archaeal exosome core and none are functional in the yeast and human exosome cores. Here, the crystal structure of the RNase PH ring from the exosome of the anaerobic methanogenic archaeon *Methanothermobacter thermautotrophicus* is described at 2.65 Å resolution. Free phosphate anions were found for the first time in the active sites of the RNase PH subunits of an exosome structure and provide structural snapshots of a critical intermediate in the phosphorolytic degradation of RNA by the exosome. Furthermore, the present structure highlights the plasticity of the surfaces delineating the polar regions of the RNase PH ring of the exosome, a feature that can facilitate both interaction with the many cofactors involved in exosome function and the processive activity of this enzyme.

1. Introduction

The exosome is a multisubunit RNA-processing machine whose core interacts with different cofactors to elicit a wealth of functions on different RNA substrates. In eukaryotes, the exosome is found in the cytoplasm as well as in the nucleus and the nucleolus. In the nucleus, the exosome edits ribosomal RNAs, small nuclear RNAs (snRNAs), small nucleolar RNAs (snoRNAs) and tRNA (Allmang *et al.*, 1999, 2000; Perumal & Reddy, 2002; Hopper & Phizicky, 2003; Kadaba *et al.*, 2004; LaCava *et al.*, 2005; Vanácová *et al.*, 2005; Schilders *et al.*, 2005). It is also involved in the degradation of aberrant mRNA and cryptic unstable transcripts (CUTs; Chanfreau, 2005; Milligan *et al.*, 2005). In the cytoplasm, the exosome is recruited by Ski7 to ribosomes stalled at mRNA 3′-ends lacking stop codons, promoting their degradation by the nonstop decay pathway (NSD; reviewed in Isken & Maquat, 2007). Ski7 can also recruit the exosome to the nonsense-mediated decay pathway (NSMD), although its role in NSMD seems to be less important than that of 3′→5′ degradation (Isken & Maquat, 2007). It has been shown that exosomes are

also recruited by the zinc-finger antiviral protein (ZAP) to degrade viral RNA, making the exosome an antiviral factor (Guo *et al.*, 2004, 2007).

Archaeal genomes contain a conserved superoperon consisting of up to 15 genes potentially related to exosome function. These genes include those encoding Rrp41 and Rrp42, which contain RNase PH (phosphorolytic) domains, and Rrp4, which contains the RNA-binding S1 and KH (protein K homology) domains (Koonin *et al.*, 2001). The first archaeal exosome complex was experimentally identified in *Sulfolobus solfataricus* (Evguenieva-Hackenberg *et al.*, 2003). The archaeal exosome has polyadenylation activity and can degrade RNA in the 3′→5′ direction. The Rrp41 protein contains a catalytic active site, while the Rrp42 subunit is catalytically inactive but is required for exosome function (Büttner *et al.*, 2005; Lorentzen & Conti, 2005). Polyadenylation in archaea seems to be restricted to those organisms that contain exosome genes, as polyadenylated RNA has not been detected in archaea lacking these genes such as halophiles and some methanogenic archaea (Portnoy *et al.*, 2005; Portnoy & Schuster, 2006). *In vitro* studies have demonstrated the polyadenylation and single-stranded RNA-degradation activities of the archaeal exosome in the presence of ADP and of nucleoside diphosphates, respectively (Büttner *et al.*, 2005; Lorentzen *et al.*, 2005; Walter *et al.*, 2006). However, despite recent work dedicated to the study of the archaeal exosome, the RNA-processing pathways that it mediates are not yet well understood, mainly owing to the lack of an appropriate model for genetic studies (Allers & Mevarech, 2005). However, it seems clear that the homologues of eukaryotic exosome regulators such as Rrp6p and Rrp47 or of the Ski proteins are not found in archaea.

A number of crystal X-ray structures of exosome complexes from hyperthermophilic archaea have been determined. They include the exosome Rrp41–Rrp42 hexamers (RNase PH rings) from *S. solfataricus* (Lorentzen *et al.*, 2005) and from *Pyrococcus abyssi* (Navarro *et al.*, 2008), the nine-subunit exosome-core complex from *S. solfataricus* (Lorentzen *et al.*, 2007), including a trimeric Rrp4 cap, and that from *Archaeoglobus fulgidus* (Büttner *et al.*, 2005), incorporating either Rrp4 or Csl4. Overall, these studies showed that the archaeal exosome core is similar to the bacterial RNase PH (Ishii *et al.*, 2003; Choi *et al.*, 2004) and PNPase (Symmons *et al.*, 2000) complexes. In addition, the structures of archaeal exosome–RNA complexes (Lorentzen *et al.*, 2007; Navarro *et al.*, 2008) have shown the path followed by RNA substrates to access the phosphorolytic active sites in the exosome core. In these structures, RNA is recognized *via* ribose-specific rather than base-specific contacts. The observation of chloride and tungstate ions bound in the phosphorolytic active site further corroborated the proposal of a catalytic 3′→5′ phosphorolytic activity mechanism for the exosome.

The structure of the human exosome core has also been solved (Liu *et al.*, 2006). Despite structural similarity, the exosome core of eukaryotes, with the notable exception of the plant lineage (Chekanova *et al.*, 2000), is catalytically inactive. Instead, RNase activities are carried out by Dis3 (Rrp44), a eukaryote-specific exosome subunit (Lebreton *et al.*, 2008; Schneider *et al.*, 2009).

We have determined the structure of the *Methanothermobacter thermautotrophicus* (*Mth*) exosome RNase PH ring, which we produced by co-expressing the mthRrp41 and mthRrp42 subunits. Notably, the structure contains free phosphate ions bound to each of the phosphorolytic active sites of mthRrp41 monomers and displays disorder in a number of functionally relevant loops. We compare this structure with other exosome structures from archaea in order to further understand the phosphorolytic mechanism as well as the role of structural plasticity in both the interaction with cofactors and in the processivity of RNA processing.

Table 1
Summary of data-collection and refinement statistics.

Values in parentheses are for the highest resolution shell.

Data collection	
Space group	$P2_12_12_1$
Unit-cell parameters (Å)	a = 89.3, b = 118.2, c = 154.7
Resolution (Å)	25.00–2.65 (2.79–2.65)
Wavelength (Å)	0.9191
Completeness (%)	98.7 (92.4)
Multiplicity	4.2 (2.5)
Unique reflections	47654 (6385)
$\langle I/\sigma(I)\rangle$	9.1 (1.5)
$R_{\rm meas}$† (%)	11.8 (58.1)
Wilson B factor (Å^2)	64.0
Matthews coefficient (Å^3 Da^{-1})	2.5
Refinement	
Protein atoms	10926
Solvent atoms (including phosphate)	140
$R_{\rm cryst}/R_{\rm free}$‡ (%)	21.1/25.1
F_o/F_c correlation coefficient§	0.94 [0.91]
R.m.s.d. (bonds)¶	0.009 [0.022]
R.m.s.d. (angles)¶	1.257 [2.002]
Average isotropic B factors (Å^2)	
Main chain	64.3
Side chains and solvent	66.2
Ramachandran plot statistics (%)	
Residues in favoured regions	96.9
Residues in allowed regions	99.9
Outliers	0.1
MolProbity score††	2.2 [94th percentile]

† $R_{\rm meas} = \sum_{hkl}[N/(N-1)]^{1/2}\sum_i|I_i(hkl) - \langle I(hkl)\rangle|/\sum_{hkl}\sum_i I_i(hkl)$ is the multiplicity-independent $R_{\rm merge}$. ‡ $R_{\rm cryst} = \sum_{hkl}||F_{\rm obs}| - |F_{\rm calc}||/\sum_{hkl}|F_{\rm obs}|$. $R_{\rm free}$ is defined as $R_{\rm cryst}$ for a test set of 973 randomly chosen reflections that were not used during refinement. § The value in square brackets is for the test-set reflections. ¶ Root-mean-square deviations from the standard values are given, with target values in square brackets. †† Reported by the *MolProbity* server (Davis *et al.*, 2007) and defined as 0.42574 × log(1 + clashscore) + 0.32996 × log{1 + max[0, %(rotamer outliers)] − 1⟩} + 0.24979 × log{1 + max[0, 100 − %(Ramachandran favoured) − 2]} + 0.5, where clashscore is the number of overlaps of >0.4 Å per 1000 atoms.

2. Materials and methods

2.1. Cloning

The *mth682* and *mth683* genes encoding the mthRrp42 and mthRrp41 proteins from *M. thermautotrophicus*, respectively, were amplified by PCR from genomic DNA with the primers 5′-CCT CA GAA **GCT AGC** ATG GTG AAT AAA ATG GAT-3′ (forward for *mth682*), 5′-AGT ATT TA**A AGC TT**A GGG AGT CAT TGA CTT GTC-3′ (reverse for *mth682*), 5′-AA TTC CGA **CAT ATG** ATT ACT ATC ATC ACA-3′

(forward for *mth683*) and 5′-AT TAT ATC **AAG CTT** ATT CAC CAT ACC TCT T-3′ (reverse for *mth683*). The reverse primers for both genes were designed to carry the *Hin*dIII restriction-enzyme site (in bold), whereas *Nhe*I and *Nde*I sites (also in bold) were included in the forward primers of *mth682* and *mth683*, respectively. The resulting products were cloned into the pET-28a expression vector (Novagen, Madison, Wisconsin, USA) to produce the pET-28a-Mth682 and pET-28a-Mth683 vectors. The *mth683* gene was further extracted from pET-28a-Mth683 using the *Nde*I and *Xho*I sites and recloned into the second multiple-cloning site of the pCDFDuet-1 expression vector (Invitrogen), producing the plasmid pCDFDuet-Mth683.

2.2. Protein expression, purification and crystallization

The mthRrp41–mthRrp42 protein complex was expressed by simultaneously transforming pCDFDuet-mth683 and pET-28a-mth682 into the *Escherichia coli* E2566 expression strain using the heat-shock method. An overnight culture of pET-28a-mth682 and pCDFDuet-mth683 co-transformed *E. coli* E2566 cells was used to inoculate fresh lysogeny broth (LB) medium. The cells were grown at 310 K to an OD_{600} of ∼0.6 and then moved to 289 K and induced for overnight expression with 2.5 m*M* isopropyl β-D-1-thiogalactopyranoside. The cells were lysed by sonication in lysis buffer (50 m*M* Tris pH 7.5, 200 m*M* NaCl) containing a protease-inhibitor cocktail. The mthRrp41–mthRrp42 complex was purified using Ni^{2+}-loaded HisTrap affinity columns (Amersham Biosciences, Chalfont St Giles, England). For crystallization purposes, the imidazole was removed from the protein by ultrafiltration using a 10 kDa cutoff concentrator and 25 m*M* Tris pH 7.5, 0.15 *M* NaCl buffer for successive dilution. The protein complex was subsequently concentrated to 11 mg ml^{-1}.

Crystals of the mthRrp41–mthRrp42 complex were obtained by hanging-drop vapour diffusion at 282 K using drops containing 1 µl protein solution and 1 µl reservoir solution equilibrated against a reservoir consisting of 5% 2-propanol, 20% PEG 3350 and 0.1 *M* succinic acid pH 7.0. Prior to flash-cooling in liquid nitrogen, crystals were transferred into a cryoprotectant solution containing 35% PEG 3350 in addition to the other crystallization reagents.

2.3. Crystal structure determination and refinement

Diffraction data from an mthRrp41–mthRrp42 crystal were collected on the BM14 beamline at ESRF (Grenoble, France) at 100 K and processed to a resolution of 2.65 Å using *MOSFLM*/*SCALA* (Collaborative Computational Project, Number 4, 1994). The structure was determined by the molecular-replacement method with the program *MOLREP* (Vagin & Teplyakov, 1997) using the structure of the RNase PH ring of the *S. solfataricus* exosome (Lorentzen *et al.*, 2005; PDB code 2br2) as a search model. The solution from *MOLREP* was improved by 25 cycles of rigid-body refinement followed by 30 cycles of restrained refinement of atomic positions and temperature factors using *REFMAC*5 (Murshudov *et al.*, 1997). The model was iteratively manually rebuilt

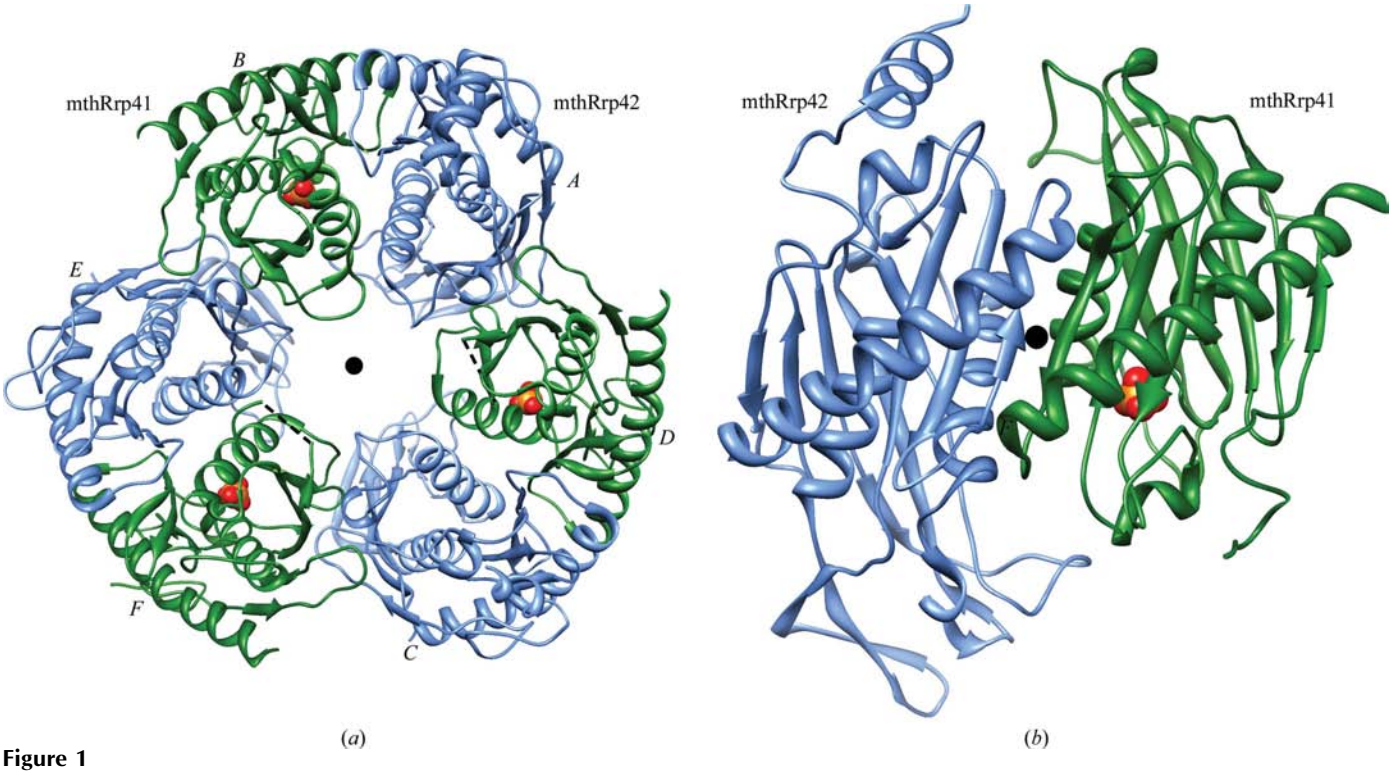

Figure 1
Overall structure of the RNase PH ring of the *M. thermautotrophicus* exosome. (*a*) Ribbon view from the KH/S1 side. mthRrp41 and mthRrp42 monomers are labelled with their respective chain identifiers. Phosphate ions bound to mthRrp41 are shown in Corey–Pauling–Koltun representation. The unmodelled neck loops of mthRrp41 chains *D* and *F* are sketched as dashed lines. The axis of the trimer is displayed as a black dot. (*b*) The mthRrp41–mthRrp42 dimer, with its pseudo-dyad axis indicated by a black dot. The axis of the trimer would be vertical and in the plane of the figure.

using *Coot* (Emsley & Cowtan, 2004) and refined with restraints, including tight noncrystallographic symmetry restraints, using *REFMAC*5. Anisotropic temperature factors were refined for TLS (translation/libration/screw) segments generated by the TLS motion-determination (*TLSMD*) server (Painter & Merritt, 2006).

3. Results and discussion

3.1. Overall structure description

We obtained crystals of the *Mth* exosome RNase PH ring belonging to space group $P2_12_12_1$. X-ray diffraction data were collected to a resolution of 2.65 Å and the structure was refined to a final R factor of 21.1% ($R_{\rm free}$ of 25.1%; Table 1). There is one hexamer per asymmetric unit, with a solvent content of 48.9%.

In the final model of the *Mth* exosome RNase PH ring, chains *B* (residues 15–236), *D* (16–61 and 73–236) and *F* (14–62 and 70–238) correspond to mthRrp41, while chains *A* (8–270), *C* (13–173 and 177–271) and *E* (21–270) correspond to mthRrp42 (Fig. 1*a*). The N-terminal 14–16 amino acids, the C-terminal 2–4 residues and the flexible-loop segments comprising residues 62–72 (chain *D*) and 63–69 (chain *F*) of mthRrp41 did not have clear electron density. The MthRrp42 chains are more complete, with the exception of seven N-terminal amino-acid residues in chain *A*, 12 in chain *C* and 20 in chain *E*, together with the respective His tags (19 residues). The loop formed by residues 174–176 of chain *C* was also found to have no clear electron density. These regions are presumably disordered. Similar to other archaeal exosomes, the *Mth* exosome RNase PH ring has a diameter of ∼95 Å and a height of ∼75 Å.

As expected, the *Mth* exosome RNase PH ring is assembled as a trimer of mthRrp41–mthRrp42 dimers arranged head-to-tail. It is, in principle, possible to define two classes of non-equivalent mthRrp41–mthRrp42 dimers. One class is represented by chain pairs *B*/*A*, *D*/*C* and *F*/*E*, while the other is made up of pairs *B*/*E*, *D*/*A* and *F*/*C* (Fig. 1*a*). In the *Mth* exosome RNase PH ring the first class of Rrp41–Rrp42 dimers is stabilized by 18 direct and seven water-mediated hydrogen bonds as well as by three salt bridges (Arg72$^{\rm mthRrp41}$–Glu239$^{\rm mthRrp42}$, Glu100$^{\rm mthRrp41}$–Arg113$^{\rm mthRrp42}$ and Asp217$^{\rm mthRrp41}$–Arg244$^{\rm mthRrp42}$). In contrast, 13 direct and three water-mediated hydrogen bonds and two salt bridges (Arg89$^{\rm mthRrp41}$–Asp140$^{\rm mthRrp42}$ and Glu177$^{\rm mthRrp41}$–Lys46$^{\rm mthRrp42}$) are involved in the second class. According to the *PISA* server (Krissinel & Henrick, 2007), the average area of the surface buried by each monomer in the first class of dimers (1336 Å^2) is just 9% larger than that of the second class (1227 Å^2). This is the smallest difference found between the two classes of Rrp41–Rrp42 dimers in archaeal exosomal

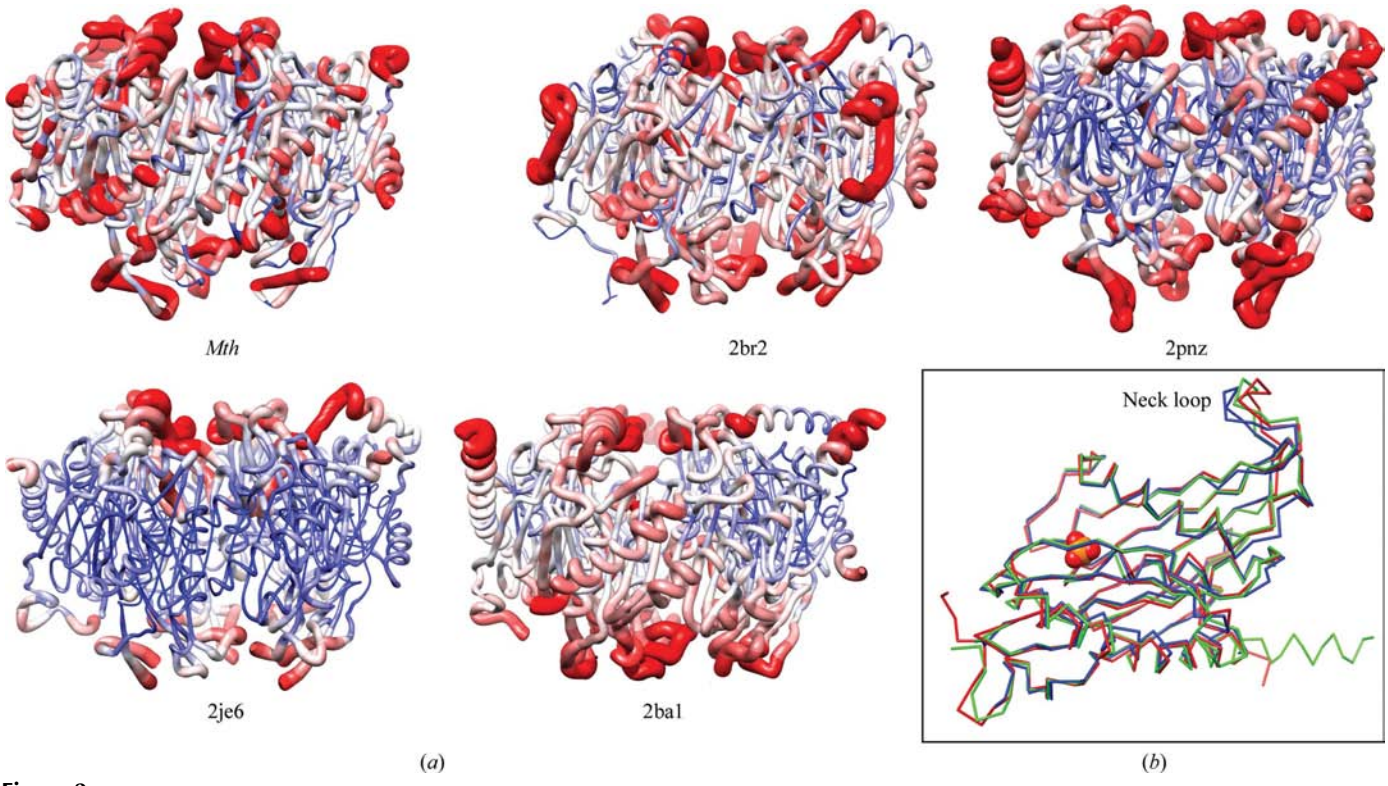

Figure 2
The flexibility of the polar sides of the exosome RNase PH ring. (*a*) The backbone structures of RNase PH rings from the *Mth*, *S. solfataricus* (PDB code 2br2), *P. abyssi* (PDB code 2pnz) exosomes and of these rings as part of the exosome nonamer complexes from *S. solfataricus* (PDB code 2ej6) and *A. fulgidus* are depicted as worms whose radii and colour (blue, low; red, high) are proportional to the residue average temperature-factor value. The KH/S1 sides are at the top and the PH-pore sides are at the bottom. (*b*) Superposition of the Rrp41 proteins from *Mth* (blue), *A. fulgidus* (green) and *S. solfataricus* (red).

RNase PH rings, which ranges from ∼22% in *P. abyssi* and *A. fulgidus* to ∼62% in *S. solfataricus*. The smaller difference arises from both a decrease in the buried area of the first class of dimers (the average for all archaeal exosome structures is 1500 Å^2) and an increase in the second one (compared with an average of 1172 Å^2). Whereas these differences may reflect sequence variations, it is worth noting that the structures of the exosome core of *A. fulgidus* obtained in the presence of two different KH/S1 cofactors, namely Rrp4 and Csl4, demonstrate that some plasticity is required in the RNase PH ring to accommodate these interactions. Whether or not flexibility plays a role in RNA degradation or polyadenylation processivity is still an open question.

3.2. The polar sides of the *Mth* exosome RNase PH ring are partly disordered

In the Rrp41–Rrp42 dimer the RNase PH domains are related by a twofold axis perpendicular to the trimer axis (Fig. 1*b*), leading to an alternate up/down disposition of the RNase PH domains in the ring. As a result, the RNase PH ring displays two different surfaces giving access to the central chamber. One of these surfaces stems from the N-termini of Rrp42 and from the Gly58–Ala73$^{\mathrm{mthRrp41}}$ and Leu113–Ser121$^{\mathrm{mthRrp41}}$ loops. This surface interacts with the KH/S1 domains of cofactors such as Rrp4 and Csl4 (Lorentzen *et al.*, 2007; Büttner *et al.*, 2005) and forms the neck of the processing chamber. The opposite surface (the PH-pore surface), which exposes the active sites of the Rrp41 monomers, originates from the N-termini of Rrp41 and from the Glu70–Gly79$^{\mathrm{mthRrp42}}$ and Ser118–Lys133$^{\mathrm{mthRrp42}}$ loops as well as the β-hairpin insertion Thr165–Lys192$^{\mathrm{mthRrp42}}$. It is interesting to note that parts of the N-termini of mthRrp41 and mthRrp42 and of the Gly58–Ala73$^{\mathrm{mthRrp41}}$ loop are not observed in the structure of the *Mth* exosome RNase PH ring, probably owing to disorder (see above). This situation is in line with the fact that the highest temperature factors of the known structures of archaeal exosomes are found in these two surfaces (Fig. 2*a*).

Such disorder and the flexibility from which it ensues are consistent with the role of the KH/S1 surface as a hub connecting the RNase PH ring to the diverse cofactors required to elicit the varied functions of the exosome. A similar role may be possible for the PH-pore surface by analogy with the eukaryotic exosome, where it interacts with the Rrp44 nuclease (Bonneau *et al.*, 2009). However, putative factors binding to the PH pore of the archaeal exosome RNase PH ring remain to be found.

The flexibility of the KH/S1 side is also required for interaction with the substrate RNA. Indeed, the neck loop Gly58–Ala73$^{\mathrm{Rrp41}}$ includes the Arg65 residue, mutation of which to glutamate (R65E$^{\mathrm{Rrp41}}$) was found to abolish RNA binding by the RNase PH ring and to reduce RNA degradation and polyadenylation by more than 90% (Büttner *et al.*, 2005). Since this arginine makes no contacts with the Rrp4 and Csl4 proteins in the exosome-core structures of *A. fulgidus* it must be implicated in the initial binding of the substrate RNA, as proposed by Lorentzen *et al.* (2007), and possibly in its relocation towards the processing chamber. In tune with these observations, the neck loop could not be fully modelled in two of the three mthRrp41 monomers. Furthermore, comparison of the sole modelled neck loop with those of other archaeal exosome structures (PDB codes 2ba0 and 2je6; Büttner *et al.*, 2005; Lorentzen *et al.*, 2007) shows a C$^{\alpha}$–C$^{\alpha}$ r.m.s.d. of ∼5 Å (Fig. 2*b*), while the r.m.s.d. for the overall molecule is only ∼1 Å. These observations strongly suggest that the neck loop can help the passage of nonstructured RNA molecules into or out of the processing chamber during exo-nucleolysis and polyadenylation, respectively.

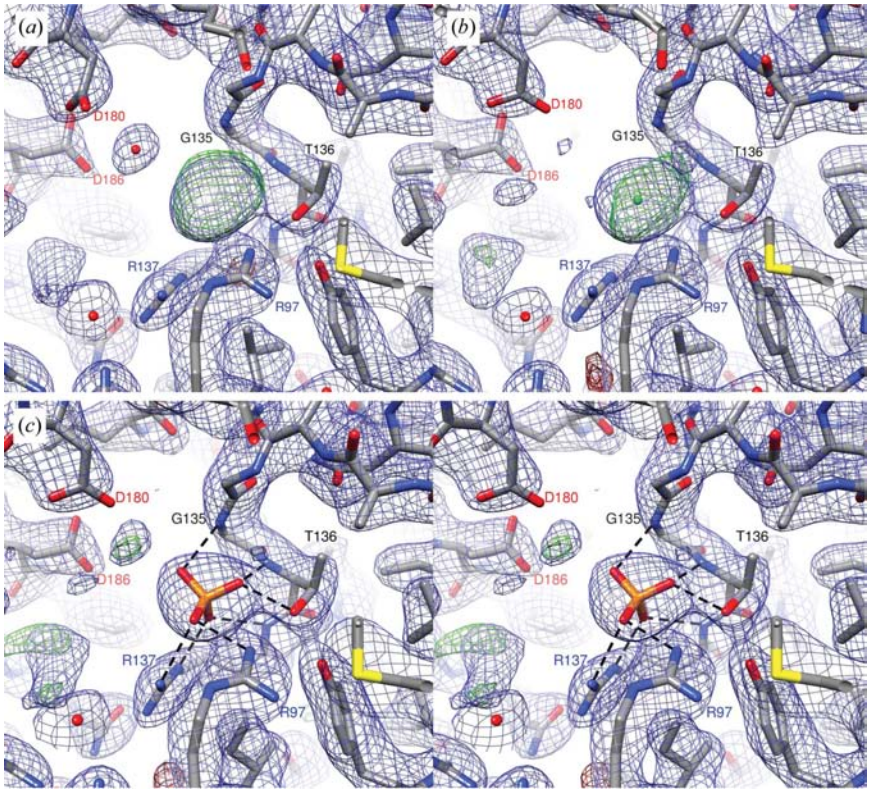

Figure 3
Phosphate bound to the active site. The mthRrp41 active site before modelling the bound ion (*a*), after modelling the difference density with a chloride ion (*b*) and a stereoview of of the final model including a phosphate ion (*c*). In (*c*), hydrogen bonds to neighbouring residues, as calculated by *Chimera*, are shown as black dashed lines. The $2mF_o - DF_c$ electron-density maps (blue) are contoured at 1σ and the $mF_o - DF_c$ difference maps (green for positive and red for negative differences) are contoured at 4σ.

3.3. Strongly bound phosphate ions in the phosphorolytic active sites of mthRrp41

During refinement of the *Mth* exosome RNase PH ring structure, the $mF_o - DF_c$ Fourier difference maps showed well

ordered electron-density peaks in the active-site pockets of the mthRrp41 molecules (Fig. 3*a*). Given the presence of chloride in the crystallization condition, chloride ions were initially modelled in the density. However, restrained refinement resulted in coordination distances of 3.5–4.0 Å to the surrounding N atoms, which were longer than the expected ∼3.3 Å corresponding to a bound chloride. Furthermore, the $mF_o - DF_c$ Fourier difference map still showed positive peaks, suggesting that chloride could not account for all the electron density present at this site (Fig. 3*b*).

The structures of other enzymes containing RNase PH domains incorporate anions bound to this pocket. Thus, chloride was found in the exosome from *S. solfataricus* (PDB codes 2c37, 2c38 and 2br2; Lorentzen & Conti, 2005; Lorentzen *et al.*, 2005), tungstate was found in the *Streptomyces antibioticus* PNPase (PDB code 1e3p; Symmons *et al.*, 2000) and phosphate was found in the RNase PH enzymes from *A. aeolicus* (PDB code 1udn; Ishii *et al.*, 2003) and *Pseudomonas aeruginosa* (PDB code 1r6m; Choi *et al.*, 2004). Moreover, the β-phosphate moiety of diphosphate nucleotides has also been found in this pocket in the exosomes from *Sulfolobus solfataricus* (PDB code 2c39; Lorentzen *et al.*, 2005) and from *Pyrococcus abyssi* (PDB codes 2pnz, 2po0 and 2po2; Navarro *et al.*, 2008). Based on this information, we decided to model this density as phosphate ions (Fig. 3*c*). We reasoned that even if phosphate was not present in the lysis, purification and crystallization buffers, phosphate ions could have been taken up from the bacterial cytoplasm and stably retained throughout purification and crystallization. Indeed, this hypothesis is consistent with the strong interaction of the modelled phosphates with main-chain amide N atoms of Gly135 and Thr136, as well as with the γ-hydroxyl of Thr136 and the guanidinium groups of Arg97 and Arg137 from the mthRrp41 molecules (Fig. 3*c*). Post-refinement analysis of *B* factors and bond distances were also compatible with the modelled phosphates. The fact that this is the first structure of an exosome hexameric core with free phosphates bound to the active sites of Rrp41 indicates that the *Mth* exosome may have a higher phosphate-binding affinity than the archaeal exosomes crystallized to date.

Therefore, the structure of the *Mth* exosome RNase PH ring represents a hitherto missing intermediate in the mechanism of phosphorolytic degradation of RNA by the exosome. We modelled a substrate RNA in the processing chamber of the *Mth* exosome RNase PH ring by superposing onto it the structure of the *P. abyssi* exosome core crystallized in the presence of a single-stranded A_{10} RNA (PDB code 2po1; Fig. 4*a*). In this model, the inorganic phosphate bound to mthRrp41 is poised to break the phosphodiester bond between nucleotides N1 and N2 of the 10-mer RNA *via* a backside attack (S_N2). In turn, $Asp180^{mthRrp41}$ is positioned so that it can act as the general acid needed to protonate the 3′-OH of the cleaved N2 ribose. This model is in keeping with the catalytic mechanism suggested previously (Lorentzen & Conti, 2005). An alternative mechanism, involving a divalent metal bound to the residues equivalent to $Asp180^{mthRrp41}$ and $Asp186^{mthRrp41}$, has recently been proposed based on the structure of *E. coli* PNPase in complex with manganese (PDB code 3gme; Nurmohamed *et al.*, 2009). The authors suggest that the metal would play a dual role, supporting the general acid–base catalysis and balancing out the charge that builds up in the transition state. The structure of the *Mth* exosome RNase PH ring is also compatible with the mechanism suggested by Nurmohamed and coworkers, since it allows the coordination of a divalent metal cation by $Asp180^{mthRrp41}$ and $Asp186^{mthRrp41}$ next to the scissile phosphate.

After the cleavage of the N1–N2 phosphodiester, the newly formed N1-diphosphate can diffuse out of the processing chamber, allowing N2 to slide towards the position previously occupied by N1. Diffu-

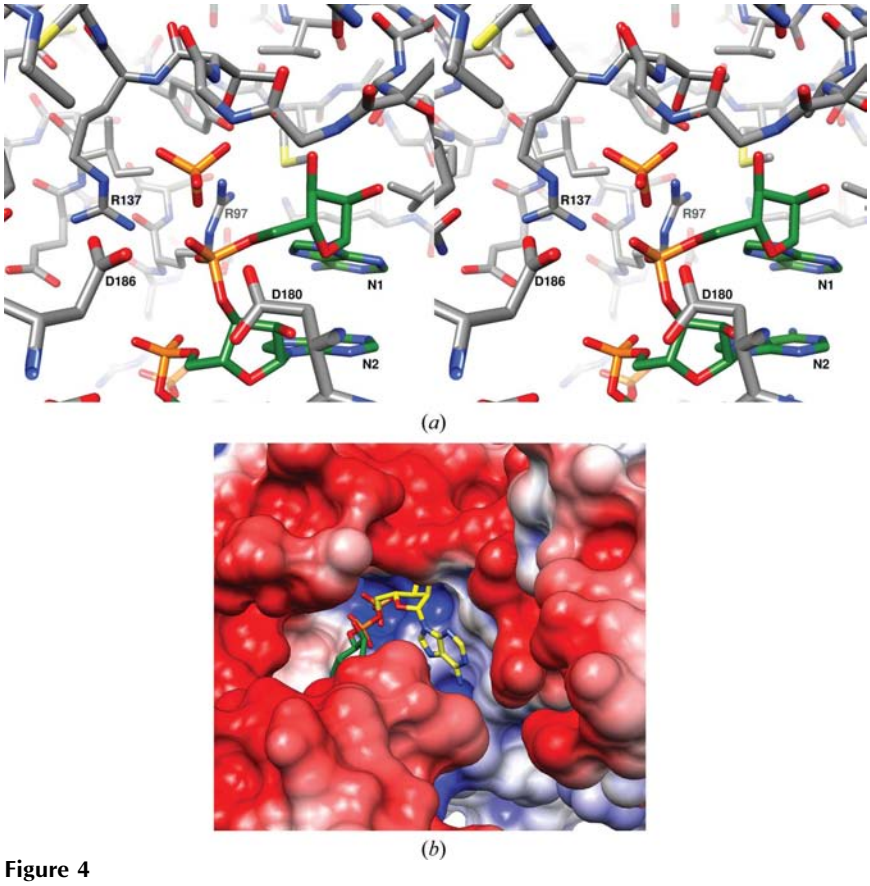

Figure 4
Possible attack and exit mechanisms in the *Mth* exosome. (*a*) RNA substrate modelled in the processing chamber of mthRrp41 using the 2po1 *P. abyssi* structure (see text for details). (*b*) A view of the modelled substrate from the PH-pore side of the RNase PH ring of the *Mth* exosome. The molecular surface is coloured by the molecule electrostatic potential calculated with *APBS* (Baker *et al.*, 2001; red, −128 mV; blue, 128 mV). C atoms from the leaving N1 nucleotide are coloured yellow.

sion of the N1-diphosphate *via* the channels associated with the PH pore is likely to be helped by the negative electrostatic potential that characterizes this side of the RNase PH ring (Fig. 4*b*) and by its flexible nature.

4. Conclusions

Exosomes are extremely versatile enzymes that need to interact with a number of different cofactors to elicit diverse functions related to RNA maturation and degradation. The structure of the *M. thermautotrophicus* exosome RNase PH ring is very similar to those of its homologues in other archaea, but it exhibits two distinctive features. This is the first exosome structure described to date that includes free phosphate ions placed in the catalytic sites, thus providing for the first time atomic detail of their binding. Furthermore, the neck loop Gly58–Ala73^{mthRrp41}, together with other elements of the N-termini of the mthRrp41 and mthRrp42 proteins, are disordered in the crystal structure, underlining the importance of their flexibility in the processivity of the exosome activities and in the recognition of the exosome cofactors.

We thank M. Chechik for her technical assistance and Dr J. Chong for providing us with genomic *Mth* DNA. This work was supported by a Wellcome Trust fellowship to AAA. We also thank the staff of the BM14 beamline at the European Synchrotron Radiation Facility (ESRF; Grenoble, France) for their help and support.

References

Allers, T. & Mevarech, M. (2005). *Nature Rev. Genet.* **6**, 58–73.
Allmang, C., Kufel, J., Chanfreau, G., Mitchell, P., Petfalski, E. & Tollervey, D. (1999). *EMBO J.* **18**, 5399–5410.
Allmang, C., Mitchell, P., Petfalski, E. & Tollervey, D. (2000). *Nucleic Acids Res.* **28**, 1684–1691.
Baker, N. A., Sept, D., Joseph, S., Holst, M. J. & McCammon, J. A. (2001). *Proc. Natl Acad. Sci. USA*, **98**, 10037–10041.
Bonneau, F., Basquin, J., Ebert, J., Lorentzen, E. & Conti, E. (2009). *Cell*, **139**, 547–559.
Büttner, K., Wenig, K. & Hopfner, K.-P. (2005). *Mol. Cell*, **20**, 461–471.
Chanfreau, G. F. (2005). *Trends Cell Biol.* **15**, 635–637.
Chekanova, J. A., Shaw, R. J., Wills, M. A. & Belostotsky, D. A. (2000). *J. Biol. Chem.* **275**, 33158–33166.
Choi, J. M., Park, E. Y., Kim, J. H., Chang, S. K. & Cho, Y. (2004). *J. Biol. Chem.* **279**, 755–764.
Collaborative Computational Project, Number 4 (1994). *Acta Cryst.* D**50**, 760–763.
Davis, I. W., Leaver-Fay, A., Chen, V. B., Block, J. N., Kapral, G. J., Wang, X., Murray, L. W., Arendall, W. B. III, Snoeyink, J., Richardson, J. S. & Richardson, D. C. (2007). *Nucleic Acids Res.* **35**, W375–W383.
Emsley, P. & Cowtan, K. (2004). *Acta Cryst.* D**60**, 2126–2132.
Evguenieva-Hackenberg, E., Walter, P., Hochleitner, E., Lottspeich, F. & Klug, G. (2003). *EMBO Rep.* **4**, 889–893.
Guo, X., Carroll, J.-W. N., Macdonald, M. R., Go, S. P. & Gao, G. (2004). *J. Virol.* **78**, 12781–12787.
Guo, X., Ma, J., Sun, J. & Gao, G. (2007). *Proc. Natl Acad. Sci. USA*, **104**, 151–156.
Hopper, A. K. & Phizicky, E. M. (2003). *Genes Dev.* **17**, 162–180.
Ishii, R., Nureki, O. & Yokoyama, S. (2003). *J. Biol. Chem.* **278**, 32397–32404.
Isken, O. & Maquat, L. E. (2007). *Genes Dev.* **21**, 1833–1856.
Kadaba, S., Krueger, A., Trice, T., Krecic, A. M., Hinnebusch, A. G. & Anderson, J. (2004). *Genes Dev.* **18**, 1227–1240.
Koonin, E. V., Wolf, Y. I. & Aravind, L. (2001). *Genome Res.* **11**, 240–252.
Krissinel, E. & Henrick, K. (2007). *J. Mol. Biol.* **372**, 774–797.
LaCava, J., Houseley, J., Saveanu, C., Petfalski, E., Thompson, E., Jacquier, A. & Tollervey, D. (2005). *Cell*, **121**, 713–724.
Lebreton, A., Tomecki, R., Dziembowski, A. & Séraphin, B. (2008). *Nature (London)*, **456**, 993–996.
Liu, Q., Greimann, J. C. & Lima, C. D. (2006). *Cell*, **127**, 1223–1237.
Lorentzen, E. & Conti, E. (2005). *Mol. Cell*, **20**, 473–481.
Lorentzen, E., Dziembowski, A., Lindner, D., Seraphin, B. & Conti, E. (2007). *EMBO Rep.* **8**, 470–476.
Lorentzen, E., Walter, P., Fribourg, S., Evguenieva-Hackenberg, E., Klug, G. & Conti, E. (2005). *Nature Struct. Mol. Biol.* **12**, 575–581.
Milligan, L., Torchet, C., Allmang, C., Shipman, T. & Tollervey, D. (2005). *Mol. Cell. Biol.* **25**, 9996–10004.
Murshudov, G. N., Vagin, A. A. & Dodson, E. J. (1997). *Acta Cryst.* D**53**, 240–255.
Navarro, M. V. A. S., Oliveira, C. C., Zanchin, N. I. T. & Guimarães, B. G. (2008). *J. Biol. Chem.* **283**, 14120–14131.
Nurmohamed, S., Vaidialingam, B., Callaghan, A. J. & Luisi, B. F. (2009). *J. Mol. Biol.* **389**, 17–33.
Painter, J. & Merritt, E. A. (2006). *Acta Cryst.* D**62**, 439–450.
Perumal, K. & Reddy, R. (2002). *Gene Expr.* **10**, 59–78.
Portnoy, V., Evguenieva-Hackenberg, E., Klein, F., Walter, P., Lorentzen, E., Klug, G. & Schuster, G. (2005). *EMBO Rep.* **6**, 1188–1193.
Portnoy, V. & Schuster, G. (2006). *Nucleic Acids Res.* **34**, 5923–5931.
Schilders, G., Raijmakers, R., Raats, J. M. H. & Pruijn, G. J. M. (2005). *Nucleic Acids Res.* **33**, 6795–6804.
Schneider, C., Leung, E., Brown, J. & Tollervey, D. (2009). *Nucleic Acids Res.* **37**, 1127–1140.
Symmons, M. F., Jones, G. H. & Luisi, B. F. (2000). *Structure*, **8**, 1215–1226.
Vagin, A. & Teplyakov, A. (1997). *J. Appl. Cryst.* **30**, 1022–1025.
Vanácová, S., Wolf, J., Martin, G., Blank, D., Dettwiler, S., Friedlein, A., Langen, H., Keith, G. & Keller, W. (2005). *PLoS Biol.* **3**, e189.
Walter, P., Klein, F., Lorentzen, E., Ilchmann, A., Klug, G. & Evguenieva-Hackenberg, E. (2006). *Mol. Microbiol.* **62**, 1076–1089.